Applied
Ceramic
TECHNOLOGY

RESEARCH ARTICLE

Electron spin resonance and photoluminescence studies of Co/Mg co-doped ZnO nanoparticles

Lutfi Arda[1] 🔟 | **Ozgul Karatas[2,3]** | **Mehmet Can Alphan[1]** | **Ersin Ozugurlu[4]**

[1]Faculty of Engineering and Natural Sciences, Department of Mechatronic Engineering, Bahcesehir University, Besiktas, Istanbul, Turkey

[2]Department of Electric and Energy, Vocational School of Technical Sciences, Konya Technical University, Konya, Turkey

[3]Department of Physics, Gebze Technical University, Gebze, Kocaeli, Turkey

[4]Department of Mathematics, Istanbul Technical University, Maslak, Istanbul, Turkey

Correspondence
Lufti Arda, Faculty of Engineering and Natural Sciences, Department of Mechatronic Engineering, Bahcesehir University, 34349 Besiktas, Istanbul, Turkey.
Email: lutfi.arda@eng.bau.edu.tr

Funding information
Research Funds of Bahcesehir University, Grant/Award Numbers: BAP.2019-01.04, BAP.2021-01.27

Abstract

$Zn_{0.95-x}Mg_{0.05}Co_xO$ ($x = 0.01-0.05$ with an increment of 0.01) nanoparticles were synthesized by using the sol–gel technique to analyze structural and magnetic properties. The single phase was observed in the X-ray diffraction measurements. To examine the surface morphology, elemental compositions, crystal quality, defect type, density, and magnetic behavior of the nanoparticles, SEM, energy dispersive X-ray analysis (EDX), PL, and ESR were used, respectively. The PL has ultraviolet and a broad emission band including violet and a blue spectral region corresponding to the defect-related and excitonic emissions. These emissions were strongly dependent on the synthesize condition and doping element and ratio. The effect of cobalt concentration on the line widths of pike to pike (ΔH_{PP}) and the g-factor of ESR spectra were investigated. By comparing the results of the ESR and PL measurements, it was determined which defect with a given g-factor was responsible for the corresponding PL emission band. In addition, ESR spectra of Mg/Co co-doped ZnO nanoparticles with different cobalt concentrations recorded at room temperature were presented. Since Mg/Co co-doped ZnO nanoparticles reveal ferromagnetism at RT, they could be an appropriate material for new devices in spin-based technologies.

KEYWORDS
defects, ESR, nanoparticles, photoluminescence properties, sol–gel method, zinc oxide

1 | INTRODUCTION

Recently, ZnO is one of the most studied semiconducting materials because it can be used in many areas such as solar cells,[1] photoelectrochemical cells,[2] gas sensors,[3] microelectronics,[4] spintronics,[5,6] light-emitting diodes,[7] and varistors.[8] Moreover, ZnO nanoparticles (NPs) also play an important role in human cells.[9] Although it can be used in so many areas, the applications of ZnO are still limited unless it is doped with different dopants/elements. Therefore, researchers are trying different transition (Co, Ni, Cu)[10–17] elements and rare earth (Eu, Er, Pr, Y, Yb)[18–21] elements to dope ZnO to control the bandgap and defects and to obtain the desired electrical, magnetic, and optical properties.

The dilute magnetic semiconductors (DMS) were obtained by doping with a small amount of transition metals (TM) (Ni, Cr, Co, Mn, V, Fe) into the ZnO.[22–28] Since Dietl et al.[29] theoretically predicted the ferromagnetic (FM) behavior at room temperature (RT) in DMS, the researchers focused on obtaining DMS materials with high Curie temperatures for spintronic applications. The properties of TM (Ni, Co, Fe, Mn, and Cr) doped ZnO were also investigated. Then, by investigating the properties of ZnO doped with deep-level (DL) impurities (Cu, As, Sn), the role of DL auxiliary additives in mediating

ferromagnetism was analyzed. Finally, for DMS compounds, it was studied by doping with Mg into ZnO to observe the relationship between the Curie temperature and semiconductor bandgap.

In the last 10 years, studies have shown that preparation conditions and methods affect FM properties.[30–35] Thus, several researchers used different methods such as chemical precipitation, thermal decomposition, RF magnetron sputtering, and sol–gel method to investigate the effect of TM (Co, Ni, Cr, Fe, and Mn) to obtain the FM behavior of ZnO.[30–35]

Chithira and John prepared cobalt-doped ZnO by a chemical precipitation method and found that for 2% Co concentration there was ferromagnetism at RT.[30]

Zong et al.[31] used a thermal decomposition method to obtain Co-doped ZnO NPs and observed that all the samples displayed remanent magnetization and ferromagnetism with nonzero coercivity at RT because of the cobalt doping and oxygen vacancies. These properties play an important role in the spintronic field.[5,6] Cobalt was also used in the fabrication of thin films by Siddheswaran et al.[36] by using the RF magnetron sputtering technique at 4% and 7% concentrations in ZnO. They observed that cobalt concentration increased the magnetization of the thin films and concluded that above 7% Co concentration ferromagnetism might be possible.

The sol–gel method was also used by Azab et al.[33] and they observed FM properties at RT. The saturation magnetization decreased as cobalt concentration in ZnO increased. For 3% cobalt concentration in ZnO, until the crystallite size reached 24 nm, the coercive field (H_c) increased but after that, it decreased because of the shift from multi- to single-domain state. They also exhibited an increase in the exchange bias by decreasing the particle size as cobalt concentration increased.

Singh et al.[34] investigated ZnCoO NPs using quantum-designed vibrating sample magnetometer (VSM) exhibiting RT ferromagnetism and high values of H_c. One year later, Pan et al.[35] used $C_2H_2O_4$ (oxalic acid) and NH_4OH (ammonium hydroxide) to synthesize $Zn_{1-x}Co_xO$ ($0.00 \leq x \leq 0.1$) NPs and the ferromagnetism behavior at RT was exhibited using VSM.

Above and many other articles in the literature pointed out that the FM moment in ZnO increased by doping of cobalt.[29,30] Transparency, high conductivity, and low cost are important features of Co-doped ZnO films.[30,37–39] This transparency vanished because of the d–d transitions of cobalt ions when cobalt concentration increased [40, and references therein].

Tamura and Ozaki[41] studied not only the magnetic properties but also the electronic density of states of ZnO NPs doped with Mn, Fe, and Co. They used SQUID to obtain the magnetization curve showing only the linear behav-

ior with no hysteresis for manganese and cobalt-doped samples.

Since zinc atoms have a radius (0.74 Å) and electronic shell close to those of cobalt atoms (0.65 Å), the lattice constant is constant when Co is doped into ZnO.

Among the several doping elements mentioned above, Mg has an impact on the bandgap energy with a value of 4 eV and higher.[42,43] Also, since the ionic radius of the Mg^{2+} ions (0.57 Å) is smaller than the Zn^{2+} ionic radius, it is simple to integrate it into the lattice of ZnO structure.[11] The blueshift appeared in ZnO when Mg concentration increased.[42] Heiba and Arda[43] concluded that the widening of the bandgap energy and achieving true blindness depended highly on the amount of high Mg content in the ZnO nanostructure. It has been observed from studies that ferromagnetism is largely dependent on growth conditions, doping elements, impurities, and defects.[29]

In this paper, to synthesize $Zn_{0.95-x}Mg_{0.05}Co_xO$ NPs ($x = 0.00$–0.05), we used the sol–gel technique. We investigated the effects of intrinsic defects such as zinc interstitial (Zn_i), zinc vacancies (V_{zn}), and oxygen vacancies (V_o) of $Zn_{0.95-x}Mg_{0.05}Co_xO$ NPs by using the photoluminescence (PL) and electron spin resonance (ESR). Moreover, the effect of Mg/Co co-doping on the magnetic and structural properties of ZnO NPs at RT was also studied.

2 | EXPERIMENTAL PROCEDURE

The $Zn_{0.95-x}Mg_{0.05}Co_xO$ NPs were prepared using the sol–gel technique by varying the doping ratio $x = 0.00$–0.05. As precursor materials, we used the composition of zinc acetate dehydrate ($Zn(CH_3CO_2)_2.2H_2O$), cobalt(II) acetate tetrahydrate ($Co(CH_3CO_2)_2.4H_2O$), magnesium acetate tetrahydrate ($Mg(CH_3COO)_2·4H_2O$). Moreover, we also used methanol (CH_3OH) and acetylacetone ($C_5H_8O_2$) to arrange clear homogenous solutions. We weighed them and then mixed all the materials with a stirrer at 300 rpm at least 5 h in the mixer without heating at RT. Then, the solvent was removed from the solution and obtained samples preheated at 200−350°C for 10 min under air, see details in refs.[2,5,6,26] As the last step, to get the preferred phases and physical possessions, we applied a 600°C temperature for each $Zn_{0.95-x}Mg_{0.05}Co_xO$ (ZnMgCoO) separately in a furnace.

The Rigaku diffractometer with Cu Kα radiation source was used to provide the structural phase definition for synthesized NPs. Using JEOL, the JSM-5910LV model scanning electron microscope (SEM) was employed to understand the microstructural possessions of the surface morphology of the samples. The Agilent Cary Eclipse Fluorescence Spectrophotometer was used to determine PL properties. We also used Jeol Mark-JES-FA300 Series ESR
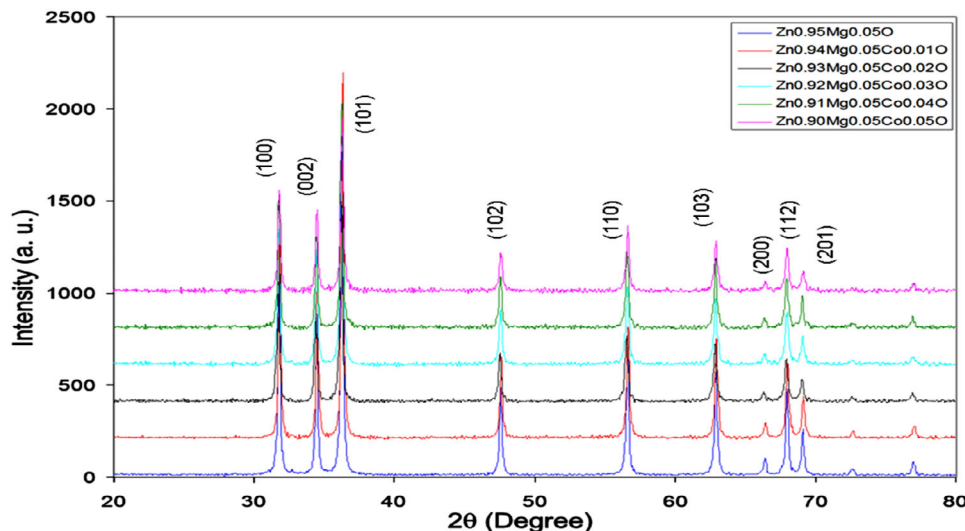
FIGURE 1 X-ray diffraction (XRD) patterns of $Zn_{0.95-x}Mg_{0.05}Co_xO$ nanoparticles.

TABLE 1 The average crystallite sizes, lattice parameters, atomic packing factor (c/a), and volume of the unit cell in $Zn_{0.95-x}Mg_{0.05}Co_xO$ ($x = 0.00$–0.05) NPs.

% Conc. (x)	D (nm)	a (Å)	c (Å)	c/a	Volume V (Å^3)
0	38.18	3.249	5.201	1.601	47.534
1	39.62	3.245	5.195	1.601	47.361
2	33.57	3.255	5.215	1.602	47.842
3	33.44	3.251	5.204	1.601	47.623
4	36.19	3.251	5.207	1.602	47.648
5	33.31	3.249	5.195	1.599	47.483

Abbreviation: NP, nanoparticle.

X-band ($\nu = 9.45$ GHz) spectrometer to obtain the ESR spectra of ZnMgCoO (annealed at 600°C) NPs. It has a DC magnetic field of up to 2 T.

In this study, a static magnetic field in the range of 0−1000 mT was used. In addition, the magnetic effects of the quartz tubes and cavity were removed from the measurements.

3 | RESULTS AND DISCUSSIONS

3.1 | Structural characterization

In Figure 1, powder patterns of $Zn_{0.95-x}Mg_{0.05}Co_xO$ ($x = 0.0$–0.05) NPs were obtained in the range of $20° \leq 2\theta \leq 80°$. As seen in Figure 1, having the highest peak index (1 0 1) in ZnMgCoO samples indicates that ZnO NPs have a preferential crystallographic (1 0 1) orientation. Besides, all ZnMgCoO samples are prepared with high quality since there was no secondary peak in Figure 1.

The structural parameters such as the crystallite size, the lattice parameters, the bond length L, etc. were calculated and illustrated in Tables 1 and 2 using X-ray diffrac-

tion (XRD) analysis and displayed in Figure 2–4A–C. The detailed formulations of δ, σ, ε, V, L, u, and D parameters were given by Guler et al.[17]

Equation (1) is used to compute the ZnO bond length:

$$L = \sqrt{\left(\frac{a^2}{3}\right) + [0.5 - u]^2 c^2},\qquad(1)$$

where the wurtzite structure u can be computed as:

$$u = \left(\frac{a^2}{3c^2}\right) + 0.25\qquad(2)$$

and Equation (3) is used to compute the lattice constants a and c of ZnMgCoO

$$\frac{1}{d_{hkl}^2} = \frac{4}{3}\left(\frac{h^2 + hk + k^2}{a^2}\right) + \frac{l^2}{c^2}.\qquad(3)$$

The Debye–Scherrer equation (4) is used to compute the average crystallite size.

$$D = \frac{K\lambda}{\beta_{hkl}\cos(\theta)},\qquad(4)$$

TABLE 2 The microstrain (ε), stress (σ), dislocation density (δ), the locality of the atoms and their displacement (u), and bond length (L) in $Zn_{0.95}Mg_{0.05}Co_xO$ ($x = 0.00–0.05$) NPs.

% Conc. (x)	ε	$\sigma*10^9$ (N/m²)	δ (nm⁻²)	U	L (Å)
0	0.000908	0.82129594	0.000686132	0.380048917	1.976634418
1	0.000875	0.297064489	0.00063692	0.380025373	1.97423181
2	0.001033	2.079451422	0.000887549	0.379810293	1.980862605
3	0.001037	1.083411665	0.000894316	0.38006529	1.977859769
4	0.000958	1.328053009	0.000763706	0.37992544	1.978195782
5	0.001041	0.332013252	0.000901295	0.380329422	1.975963477

Abbreviation: NP, nanoparticle.
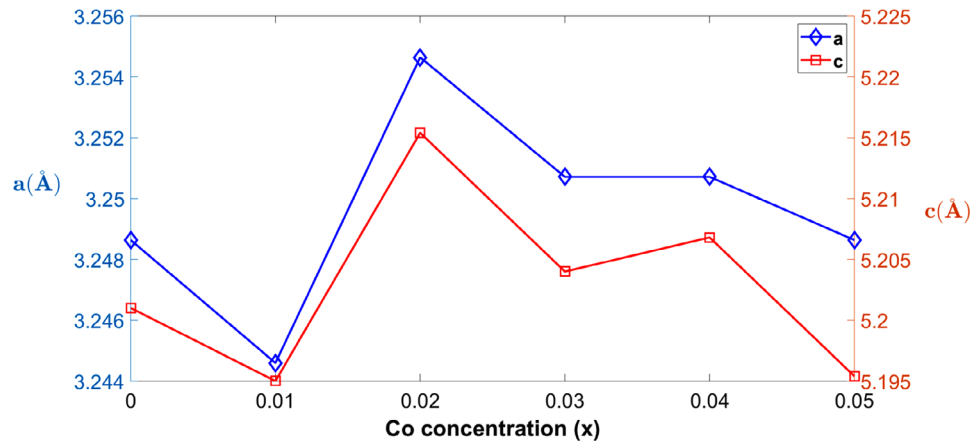
FIGURE 2 The lattice parameters (a and c) vs. Co concentration for $Zn_{0.95−x}Mg_{0.05}Co_xO$ structures.
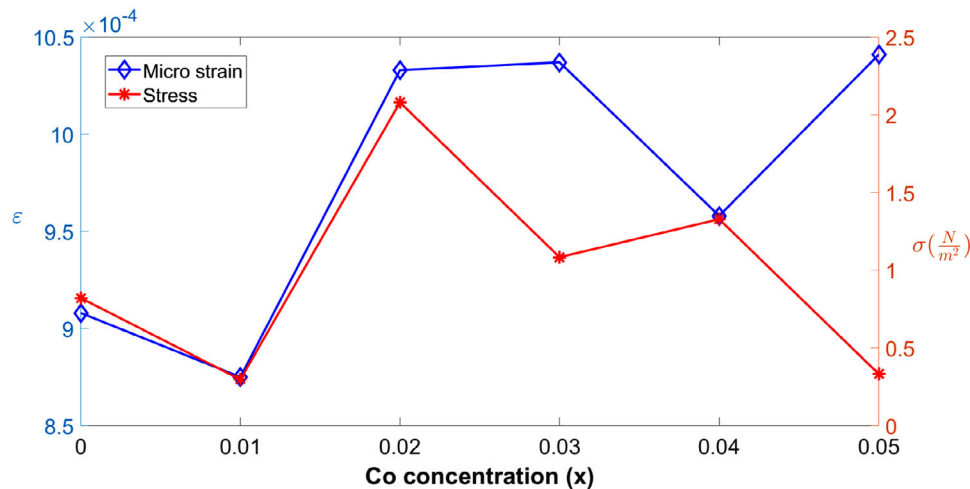
FIGURE 3 The microstrain (ε) and stress (σ) vs. Co concentration for $Zn_{0.95−x}Mg_{0.05}Co_xO$ structures.

where the integral half-width is β_{hkl}, $K = 0.90$, the wavelength λ of the incident X-ray ($\lambda = 0.1540$ nm), and the Bragg angle is θ. Figure 2 illustrates that a and c lattice parameters have a similar pattern meaning that no change in the crystal structure by the cobalt content.[28]

After 2% Co concentration, the microstrain ε and stress σ oscillate in opposite directions as shown in Figure 3.

In the crystal structures as shown in Figures 3 and 4, an increment in physical defects and dislocations might be due to the strain and stress forces. Therefore, when the strain attains its maximum (minimum), the dislocation density also becomes maximum (minimum). Bond length L oscillated as Co concentration was increased, as shown in Figure 4A. An inverse behavior was detected between the
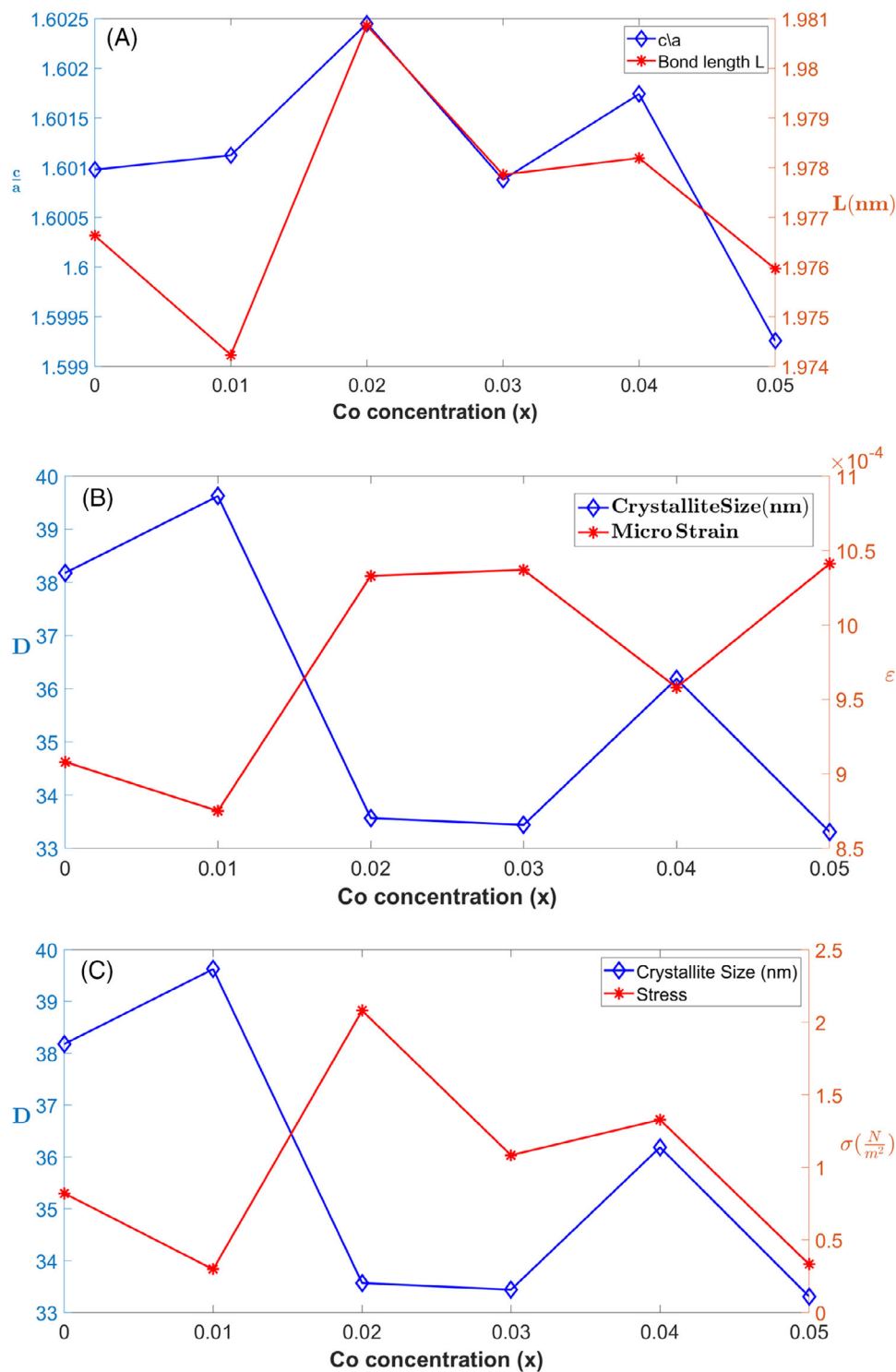
FIGURE 4 (A) The lattice parameters (c/a) and Zn–O bond lengths (L) vs. Co concentration for $Zn_{0.95-x}Mg_{0.05}Co_xO$ structures. (B) The crystallite size (D) and microstrain (ε) vs. Co concentration for $Zn_{0.95-x}Mg_{0.05}Co_xO$ structures. (C) The crystallite size (D) values and stress (σ) variation vs. Co concentration for $Zn_{0.95-x}Mg_{0.05}Co_xO$ structures.

crystallite size D and microstrain ε values as cobalt concentration was increased, as depicted in Figure 4B. The crystallite size D and the unit cell volume V oscillated as Co concentration was increased, as shown in Figures 4C and 5, respectively.

We used SEM for the morphology and energy dispersive X-ray analysis (EDX) for the elemental concentration of all $Zn_{0.95-x}Mg_{0.05}Co_xO$ NPs as displayed in Figures 6–11 and Figures 6D–11D, respectively. When the EDX graph is examined, the presence of only Zn, Co, and Mg peaks
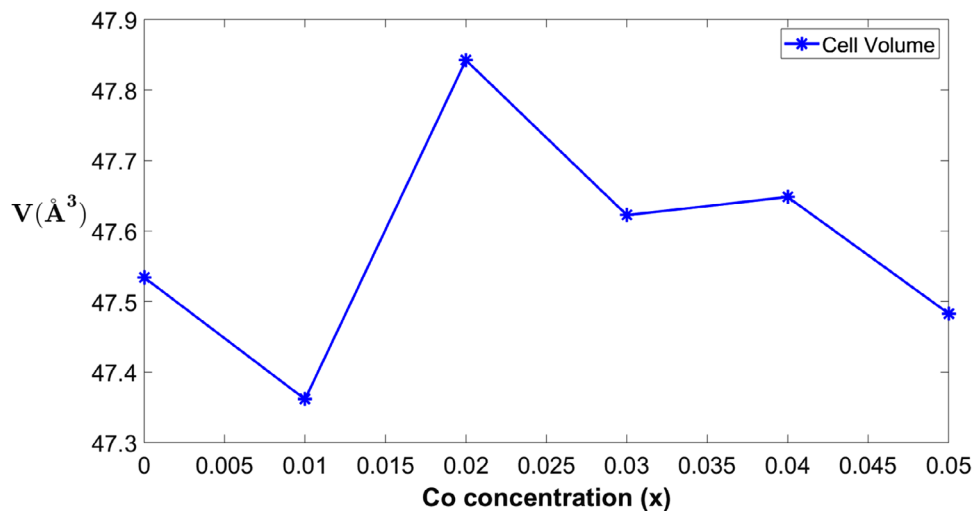
FIGURE 5 The unit cell volume vs. Co concentration for $Zn_{0.95-x}Mg_{0.05}Co_xO$ structures.

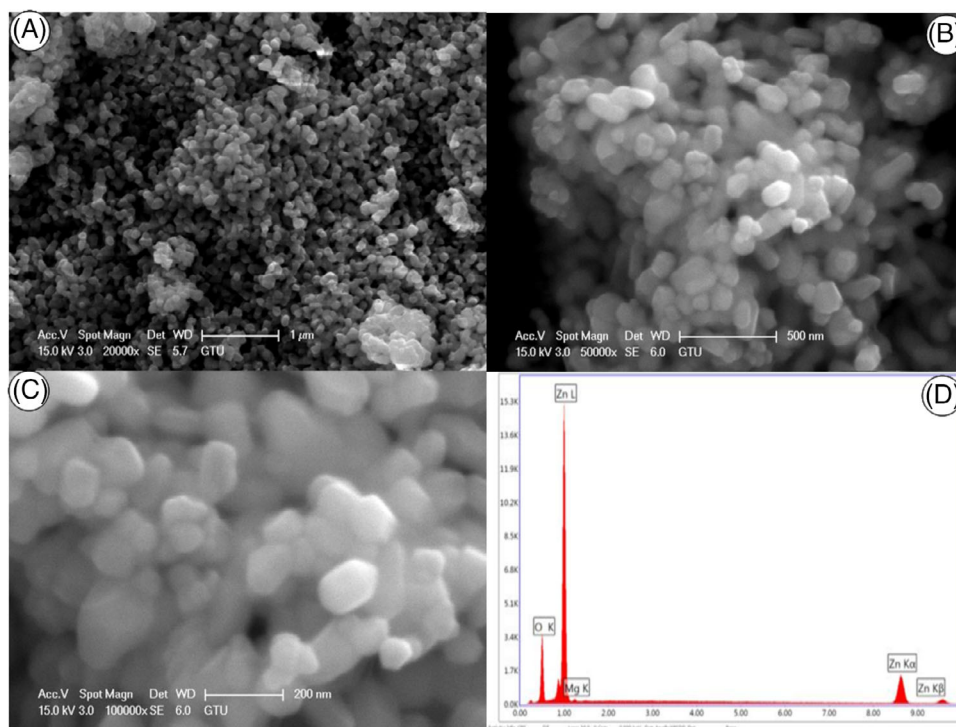**FIGURE 6** The SEM images of $Zn_{0.95}Mg_{0.05}O$ composition (A) 1 μm, (B) 500 nm, (C) 200 nm, and (D) the EDX graph of $Zn_{0.95}Mg_{0.05}O$ sample. SEM, scanning electron microscope.

shows that there are no extra elemental peak contributions. Figures 6–11 illustrate that the particle distributions within the range of 1 μm, 500 nm, and 200 nm magnifications were compact, quasi-spherical, melted, and agglomerated as illustrated in the SEM micrographs. The average crystallite sizes which were calculated and illustrated in Table 1 are compatible with the SEM images. As the Co concentration increases agglomeration increases, the surface morphology of the NPs looks sponge-like, and NPs become denser. Figure 12A,B shows the transmission elec-

tron microscope (TEM) image of the $Zn_{0.93}Mg_{0.05}Co_{0.02}O$ NPs with different magnifications (20–50 nm).

3.2 | Photoluminescence

PL spectra are used to observe the crystal feature, deficiency type, and imperfection density of semiconductor materials. Therefore, we investigated the effect of Mg/Co concentration on the PL properties of ZnO NPs by using
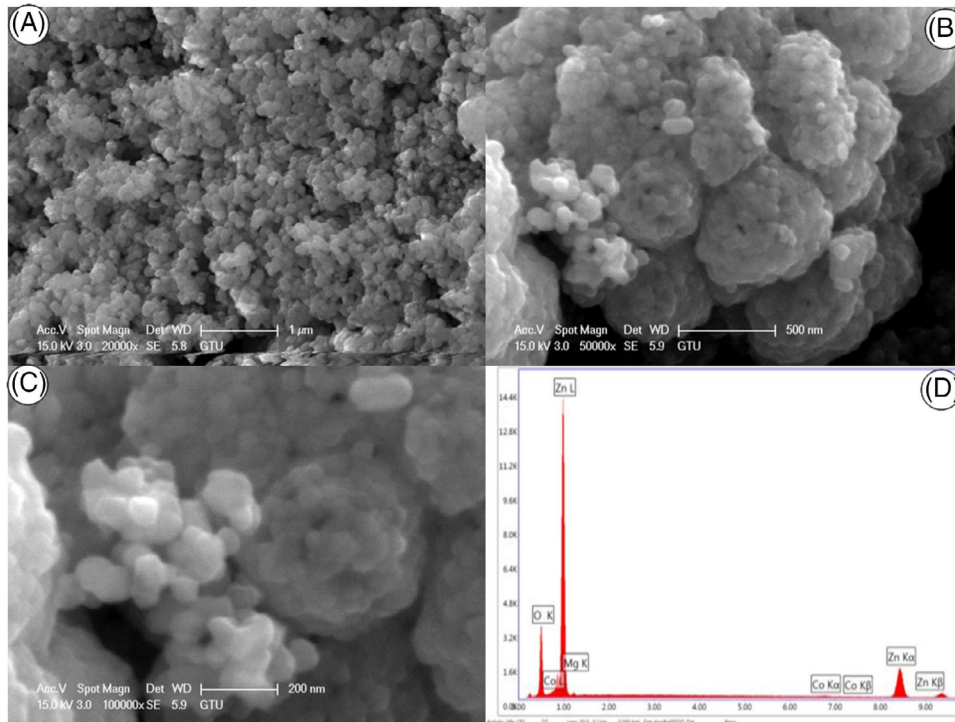
FIGURE 7 The SEM images of $Zn_{0.94}Mg_{0.05}Co_{0.01}O$ composition (A) 1 μm, (B) 500 nm, (C) 200 nm, and (D) the EDX graph of $Zn_{0.94}Mg_{0.05}Co_{0.01}O$ sample. SEM, scanning electron microscope.
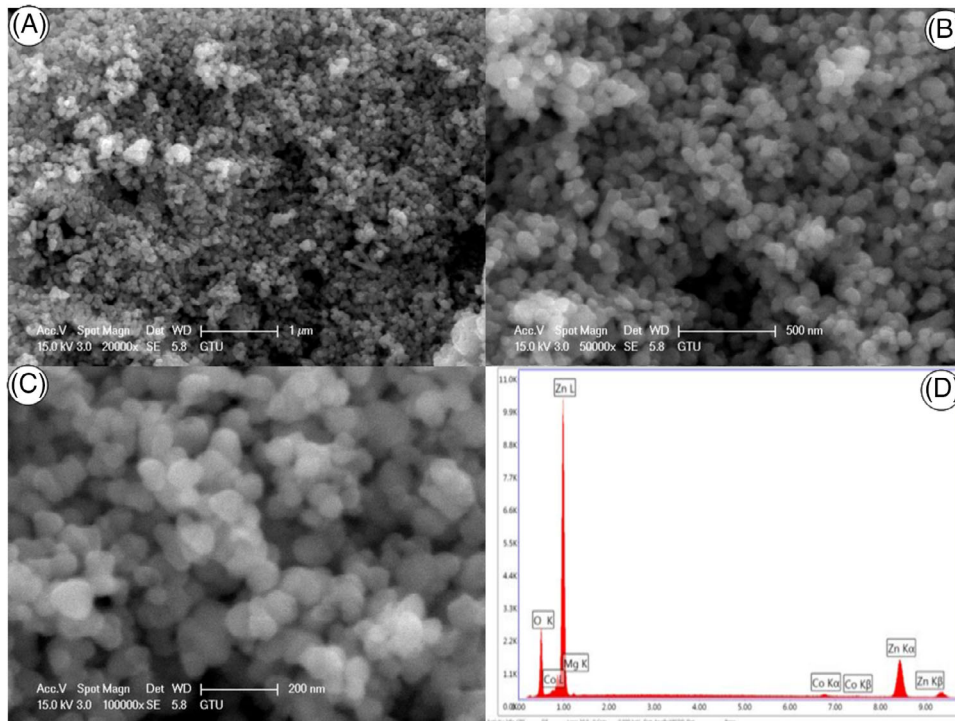

FIGURE 8 The SEM images of $Zn_{0.93}Mg_{0.05}Co_{0.02}O$ composition (A) 1 μm, (B) 500 nm, (C) 200 nm, and (D) the EDX graph of $Zn_{0.93}Mg_{0.05}Co_{0.02}O$ sample. SEM, scanning electron microscope.
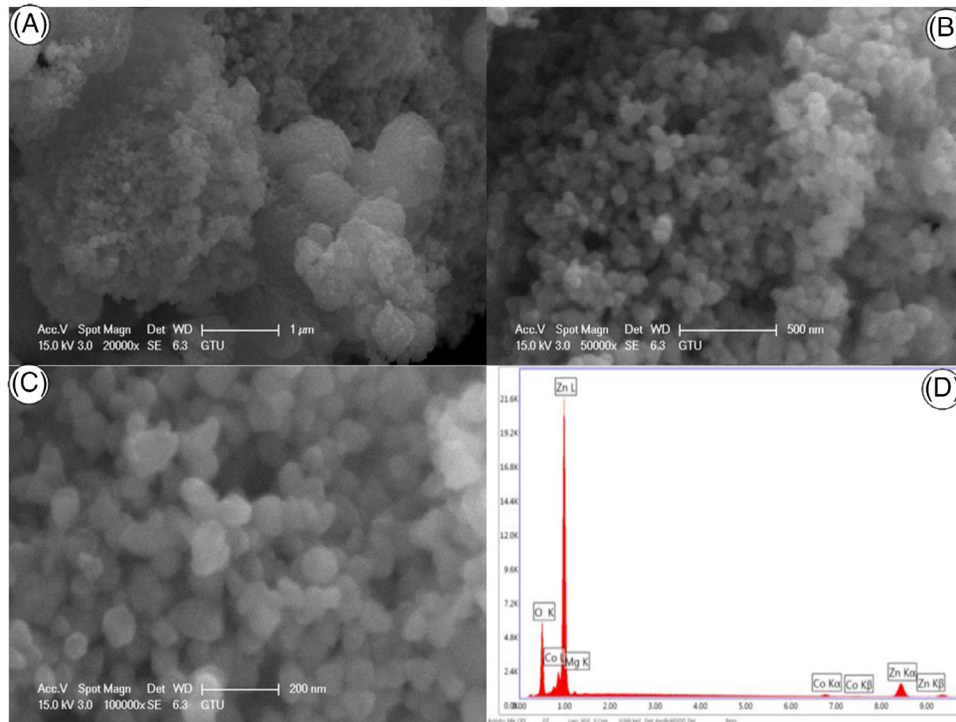
FIGURE 9 The SEM images of $Zn_{0.92}Mg_{0.05}Co_{0.03}O$ composition (A) 1 μm, (B) 500 nm, (C) 200 nm, and (D) the EDX graph of $Zn_{0.92}Mg_{0.05}Co_{0.03}O$ sample. SEM, scanning electron microscope.
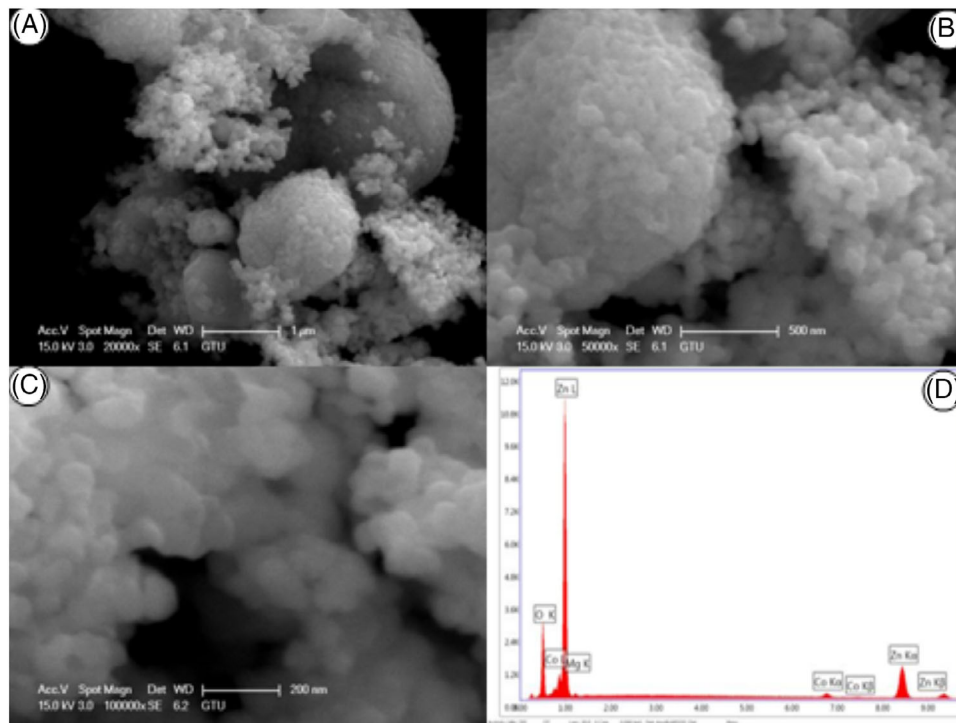

FIGURE 10 The SEM images of $Zn_{0.91}Mg_{0.05}Co_{0.04}O$ composition (A) 1 μm, (B) 500 nm, (C) 200 nm, and (D) the EDX graph of $Zn_{0.91}Mg_{0.05}Co_{0.04}O$ sample. SEM, scanning electron microscope.
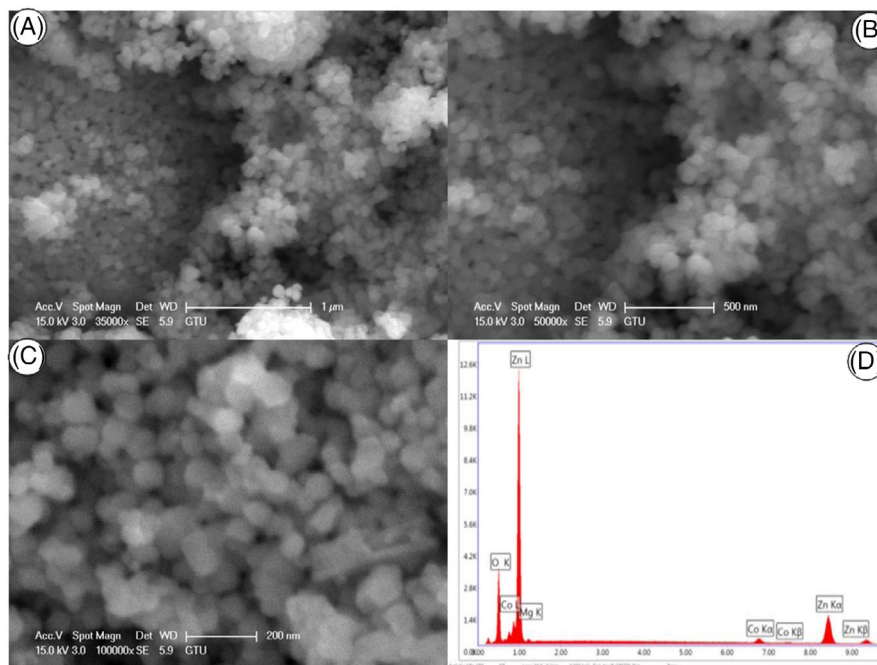
FIGURE 11 The SEM images of $Zn_{0.90}Mg_{0.05}Co_{0.05}O$ (A) 1 μm, (B) 500 nm, (C) 200 nm, and (D) the EDX graph of $Zn_{0.90}Mg_{0.05}Co_{0.05}O$ sample. SEM, scanning electron microscope.
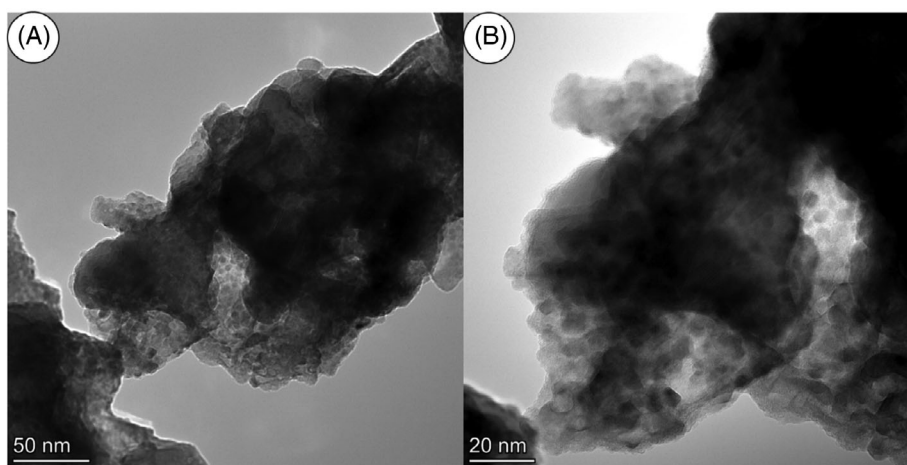

FIGURE 12 (A,B) Transmission electron microscope (TEM) images of $Zn_{0.93}Mg_{0.05}Co_{0.02}O$ nanoparticles under different magnifications.

PL. We obtained PL measurements of Mg/Co co-doped ZnO NPs at 300 nm excitation wavelength, and the emission lines were collected in the wavelength range (350–900) nm as depicted in Figure 13. The PL value of all NPs has reached its maximum value of around 380 nm as shown in Figure 13. As the Co concentration changes, it is seen that the shifts in the peaks and the intensity of the peaks change. Two dominant emissions peaks, which correspond to the typical n-type ZnO semiconductor, a sharp ultraviolet emission peak, and a broad visible emission band are seen. It is known that ultraviolet emission is responsible for crystallization quality and the number of

defects of ZnO, while visible region emission is caused by defects.[44]

The ultraviolet region generally was attributed to the near band edge (NBE) transition as a common optical property of a wide bandgap of ZnO. NBE emission originated from the excitonic transitions between electrons and holes, in the conduction band (CB) and the valance band, respectively.[44] The stronger ultraviolet emission is observed in ZnO with higher crystallization quality and lesser defect.

It is seen that NBE emission does not change with Co concentration, only a shift is observed in the peaks.
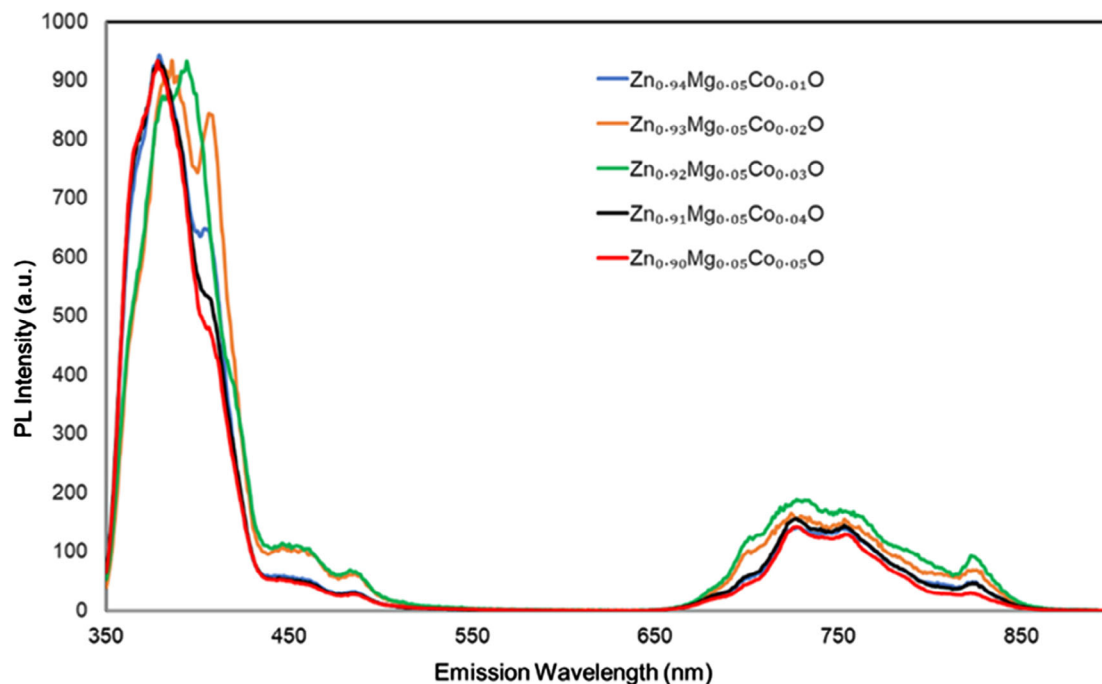
FIGURE 13 PL spectra of $Zn_{0.95-x}Mg_{0.05}Co_xO$ (x = 0.01, 0.02, 0.03, 0.04, 0.05) nanoparticles. PL, photoluminescence.

Also, it is seen that a high crystal structure is obtained by annealing at 600°C which is a suitable temperature.[43] The second dominant broad emission band is a visible region, which consists of violet–blue–green–yellow–orange, red, and near-infrared (NIR). This visible emission also known as the DL emission is assigned to impurities or defects including oxygen vacancies (V_o), zinc interstitial (Zn_i), zinc vacancies (V_{zn}), oxygen antisite (O_{zn}) and oxygen interstitial (O_i) in the ZnO crystal structure.[44,45] We observed violet, blue red, and NIR emission peaks which were explained in detail by using the Gaussian decomposition into the subpeaks according to their origin to understand the defects that occurred. The 12 main Gaussian decompositions of PL spectra were exhibited versus emission wavelength for Co concentration as shown in Figure 14. The peak labels with position center and height of the different Co concentrations of ZnMgO NPs are indicated in Table 3. Emissions of these peaks are (Peaks 1 and 2) two ultraviolet emissions, (Peaks 3, 4, and 5) three violet emissions, (Peaks 6 and 7) two blue emissions, (Peak 8, Peak 9, and Peak 10) three red emissions, and (Peak 11 and Peak 12) two NIR peaks as shown in Table 3. The emission regions, which are shown in Table 3, could be explained as the following: ultraviolet emissions from 362 to 390 nm could be ascribed to the NBE of ZnMg-CoO as an indication of the excitonic characteristic; violet emissions at (390−450 nm) region are due to the transition of electrons to the valence band (VB) from zinc interstitials-Zn_i with different charges, including neutral-Zn_i, single-Zn_i', and double-Zn_i'', respectively. According to the theoretical study by Singh and Gopal.[46] shal-

low donor levels of neutral-Zn_i, single-charged-Zn_i', and double-charged-Zn_i'' are positioned at 0.22–0.5 eV below the CB, respectively as shown in Figure 15; blue emission (450–495 nm) could be attributed to the Zn vacancies (V_{Zn}) and the red emission (690–750 nm) could be ascribed to oxygen vacancies (V_O), respectively. The NIR region (750–826 nm) was related to the secondary UV diffraction. Peaks 11 and 12 which are NIR emission were observed by Senol et al.[47] and it could be caused by oxygen vacancies. According to the results of the Gaussian decompositions of PL spectra, the illustrative energy level diagram showing the transitions between the VB and CB is shown in Figure 15.

3.3 | Electron spin resonance studies

Magnetic NPs or magnetic nanomaterials consisting of atoms, molecules, or those with electronic or nuclear magnetic moments can be described as a spin system. It causes the spin system to absorb energy from the applied electromagnetic wave. Magnetic resonance spectroscopy examines the magnetic properties of the spin system based on this absorbed energy and is divided into two groups, namely, ESR) or electron paramagnetic resonance (EPR) spectroscopy (deals with transitions between electronic spin energy levels) and nuclear magnetic resonance (NMR) (deals with transitions between energy levels of nuclear spin).

A trace of the magnetic center can be explained in ESR resonance spectra which can show many rich properties.
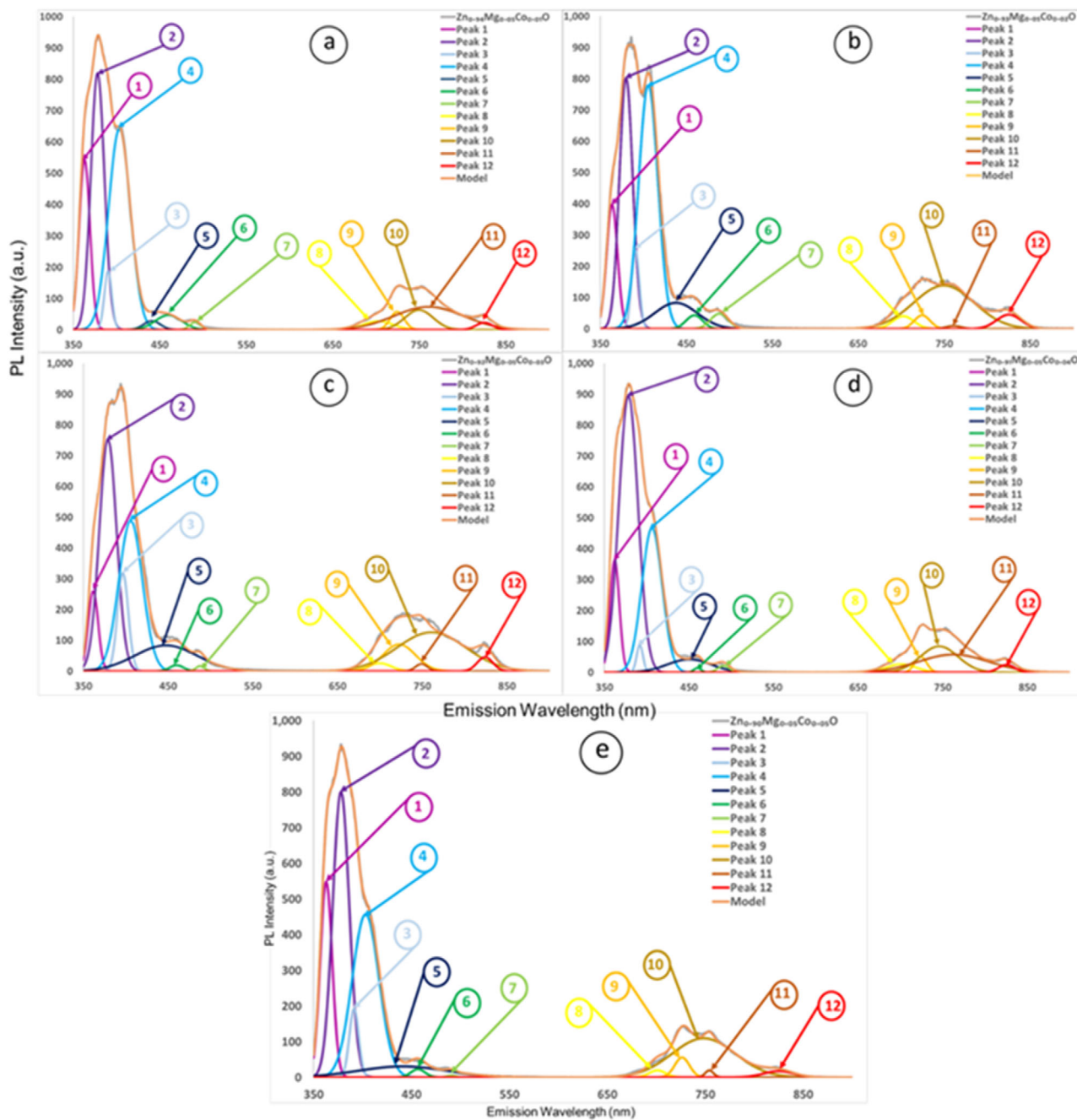
FIGURE 14 From top to the right: Gaussian decompositions of PL spectra of $Zn_{0.95-x}Mg_{0.05}Co_xO$ (A) Co (%1), (B) Co (%2), (C) Co (%3), (D) Co (%4), and (E) Co (%5) nanoparticles. PL, photoluminescence.

Especially, the ESR also helps us to identify a site occupied by ion vacancy or magnetic ions. The properties of the ESR resonance spectrum are combined with the spin Hamiltonian H of a magnetic center given by

$$H = S.g_e.H + H_{cf} + S.D.S + S.A.I + I.g_n.H + S.J.S + JS_1.S_2. \tag{5}$$

In Equation (5), the first term represents the static Zeeman effect, the last term indicates dipolar and exchange interactions of the spins located at various sites, and the other terms are spin–spin interactions, spin-dependent crystalline energy (fine structure), hyperfine interactions between electronic and nuclear spins of a site, spin–orbit interaction, and even nuclear Zeeman interaction, etc.

The Zeeman effect (first term) shows itself both in the modification of any significance peak and its line broadening. The last term which is exchange interaction governs all other terms in the FM situation, it can be neglected for the dilute distribution of spins through a paramagnetic situation. As reference [18, and references therein] is given, the nuclear Zeeman and hyperfine terms are weaker compared to the other terms. Moreover, the fine configuration

TABLE 3 The height values and peak center, emission range, and origin of PL emission of the Mg/Co co-doped ZnO NPs.

Peak Label	Co (%1)		Co (%2)		Co (%3)		Co (%4)		Co (%5)		Emission Range	Emission Origin	
	Center	Height	Center	Height	Center	Height	Center	Height	Center	Height			
Peak 1	362.9	543.8	363.6	396.9	361.6	260.4	362	363.7	363.0	548.9	Ultraviolet	Exciton	NBE Emission
Peak 2	378.0	820.9	379.9	803.4	379.0	753.0	378	894.8	378.0	801.0	Ultraviolet	Exciton	
Peak 3	390.1	188.2	390.6	253.8	396.6	318.7	392	89.3	391.3	193.3	Violet	$(Zn_i) \rightarrow (V_B)$	DL Emission
Peak 4	403.3	641.3	405.7	779.7	405.8	489.0	406	467.4	403.1	457.1	Violet	$(Zn_i) \rightarrow (V_B)$	
Peak 5	440.8	28.8	437.9	83.5	447.4	83.9	450	42.9	440.8	31.6	Violet	$(Zn_i) \rightarrow (V_B)$	
Peak 6	460.0	47.1	459.3	43.5	460.0	19.6	460	15.0	456.6	23.4	Blue	(V_{Zn})	
Peak 7	490.8	24.9	488.3	48.6	487.8	16.5	491	21.2	490.8	6.1	Blue	(V_{Zn})	
Peak 8	702.4	27.4	702.3	40.7	699.7	25.7	701	27.5	701.07	20.04	Red	(V_o)	
Peak 9	724.2	58.5	724.1	43.6	722.7	87.3	724	51.4	726.31	56.18	Red	(V_o)	
Peak 10	749.5	64.3	749.6	138.9	760.7	126.9	746	84.8	748.39	109.75	Red	(V_o)	
Peak 11	760.9	73.5	760.8	10.0	749.0	24.1	763	57.9	754.16	20.10	NIR (near-infrared)	(V_o)	
Peak 12	825.0	23.4	825.1	45.6	824.0	45.6	825.4	24.4	824.96	18.06	NIR (near-infrared)	(V_o)	

Abbreviation: PL, photoluminescence; NP, nanoparticle.
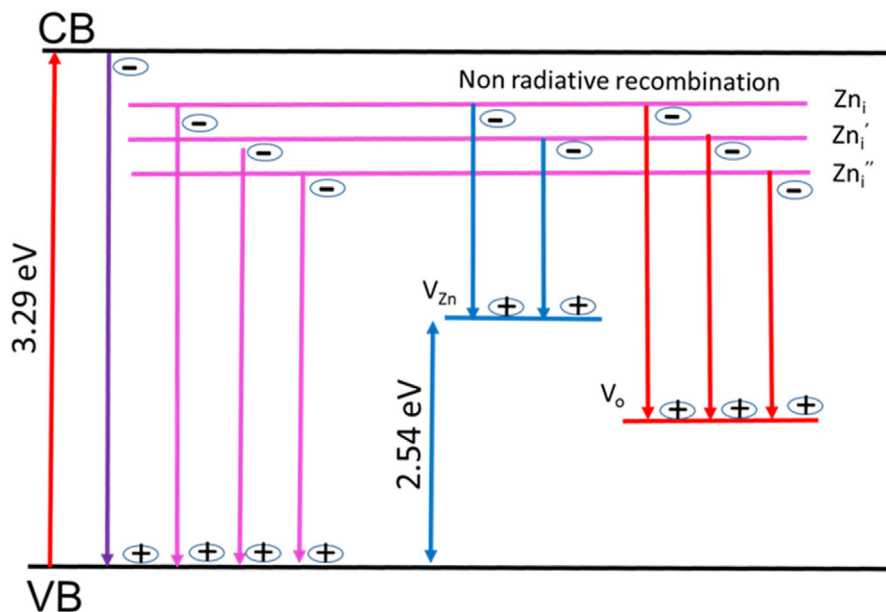
FIGURE 15 Schematic energy diagram of Mg/Co-doped ZnO nanoparticles.

terms can result in multiple resonance lines for a total spin of $S = 1$ or higher.[47]

ESR spectra of Mg/Co co-doped ZnO NPs were recorded as the first derivative of the absorption signal at RT. The DC magnetic field was perpendicular to the sample tubes which were parallel to the microwave magnetic field. The spectrometer was set as follows: the microwave power was 5 mW and the magnetic field modulation was 100 kHz. In the ESR curve, we plotted the field derivative of power absorption intensity versus the external mag-

netic field in Figure 16. Figure 16 shows the ESR spectra of $Zn_{0.95-x}Mg_{0.05}Co_xO$ (where $x = 0.01$–0.05) NPs in the field region of 300–350 mT. Before we plotted the spectra, the subtraction of background input originating from the microwave cavity and empty sample tube was done. The cobalt concentration is exhibited in Figure 16 for each sample. By comparing all spectra, we observed relatively only one single, narrow, and weak resonance peak in these ranges and ESR peak intensity changed with cobalt concentration, since a single hole/electron may have a half
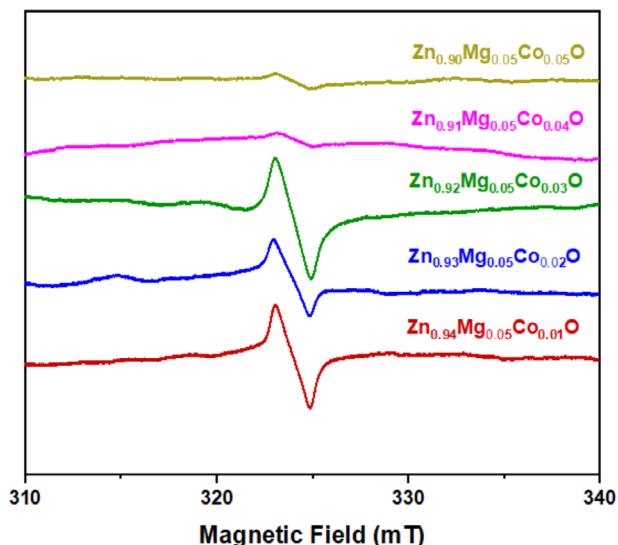
FIGURE 16 ESR spectra of all samples $Zn_{0.95-x}Mg_{0.05}Co_xO$ ($x = 0.01$–0.05). ESR, electron spin resonance.

spin and give two energy levels (for a spin down and up circumstances) separated by the Zeeman effect as mentioned above. In the tail of the ESR spectra, we also observed very small peaks. The peak intensity significantly decreased as Co concentration increased.

3.4 | Magnetic analysis

At RT, to investigate the magnetic components, the ESR measurements were taken as illustrated in Figure 16. Figure 16 showed a broad single resonance peak which is a clear signature of FM nature. We calculated the line widths of peak-to-peak (ΔHPP) and the g-factor by using the ESR spectra. The ESR spectra and scaled experimental X-band-

ESR spectra of $Zn_{0.95-x}Mg_{0.05}Co_xO$ NPs annealed at RT were shown in Figure 16. Figure 16 displayed the widest and strong signal at about 320 mT. Cobalt concentration changed the intensity of the ESR peak and the highest peak appeared at 1% Co concentration. The peak intensities decreased significantly as Co concentration increased because of the number of increasing Zn vacancies. Some of the peaks related to the tail of the ESR spectra mentioned above occurred due to the oxygen vacancies which were also illustrated in the PL analysis. Table 3 illustrates the asymmetry factor (P_{asy}) values according to the following formula:

$$P_{asy} = 1 - \frac{h_u}{h_L}, \qquad (6)$$

where h_L and h_u are the heights of the absorption peak below and above the baseline of the ESR spectra, respectively, see Guler et al.[17] In addition, the number of spins (N_s) can be calculated as the following formula:

$$N_s = 0.285 \times I_{pp} \times (\Delta H_{pp})^2, \qquad (7)$$

where I_{pp} and ΔH_{pp} are the peak-to-peak intensity and line widths, respectively.

At 3% Co concentration, P_{asy} had an absolute minimum and N_s was maximum. We analyzed the g-factor and ΔH_{pp} to understand the ESR spectra spins' relaxation mechanism.

We only used 34 data points in the cubic spline interpolation for the original 65 535 data points of each ESR spectra curve as shown with the dotted lines in Figure 17. In these approximations, the relative errors were 0.1171, 0.0892, 0.0544, 0.0909, and 0.2032 for $Zn_{0.95-x}Mg_{0.05}Co_xO$ (($x = 0.01$–0.05) NPs, respectively. ΔH_{pp} values of the ESR

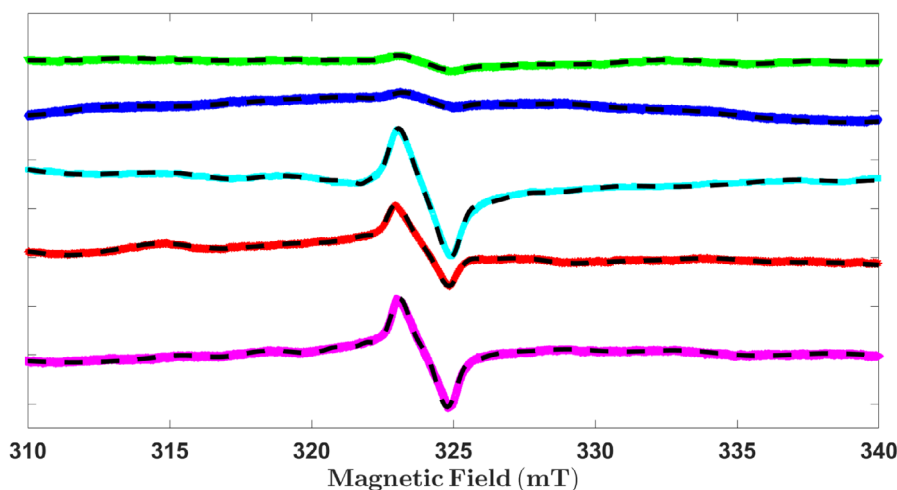**FIGURE 17** ESR spectra (solid lines) and scaled experimental X-band-ESR spectra (dotted lines) of $Zn_{0.95-x}Mg_{0.05}Co_xO$ [$x = 0.01$ (purple), 0.02 (red), 0.03 (cyan), 0.04 (blue), and 0.05 (green)] nanoparticles at RT. ESR, electron spin resonance; RT, room temperature.

TABLE 4 The ESR parameters for $Zn_{0.95-x}Mg_{0.05}Co_xO$ ($x = 0.01–0.05$) NPs.

Co (%)	h_L	h_U	P_{asy}	N_s	I_{pp}	g-values	Line-widths (ΔH_{pp})
1	−1082.762	1158.251	2.070	2113.036	2241.013	2.09030	1.819
2	−592.896	1074.137	2.812	1733.954	1667.033	2.08930	1.910
3	−1986.127	629.8730	1.317	2617.755	2616.000	2.09132	1.874
4	58.359	381.3760	−5.535	331.1477	323.017	2.08797	1.897
5	−190.385	153.2960	1.805	285.5426	343.681	2.09218	1.707
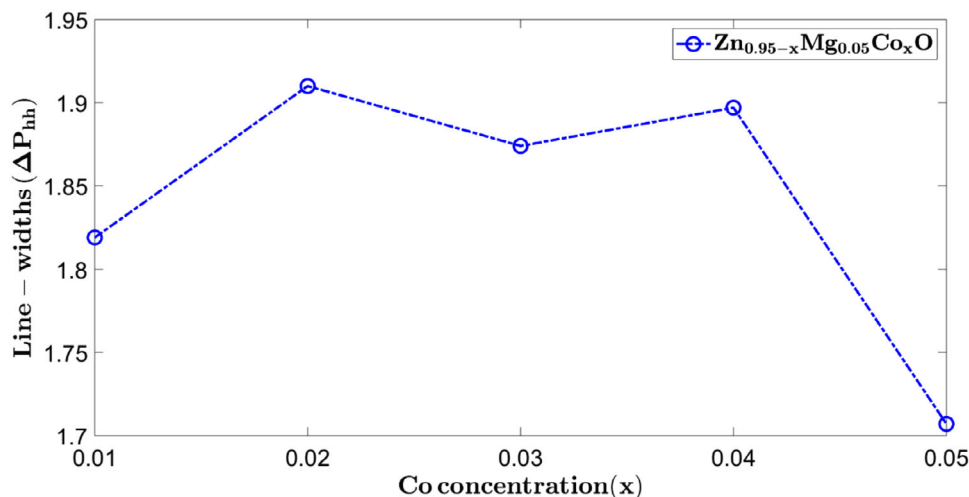
FIGURE 18 ΔH_{pp} of ESR spectra of $Zn_{0.95-x}Mg_{0.05}Co_xO$ ($x = 0.01–0.05$ with an increment of 0.01) nanoparticles vs. Co concentrations. ESR, electron spin resonance.

signals were found to be in the range of 1.7074 and 1.9104 mT as illustrated in Table 4 and Figure 18. We used the following formula to get the g-factor values:

$$h\nu = g\mu_\beta H, \qquad (8)$$

where Planck's constant is h, the operating frequency of the X-band spectrometer is ν which is 9.45 GHz, μ_β is the electron Bohr magneton, and H is the applied magnetic field. The standard g_e value for the electron is 2.00232. Solving Equation (8) for the electron Bohr magneton and plank constant gives:

$$g = 71.4477\nu/H. \qquad (9)$$

Using Equation (9), the g-factor was calculated and plotted as shown in Figure 19.

Note that $g > 2$ is an indication of a FM behavior of the ZnMgCoO NPs as depicted in Figure 20 which may be explained as a result of Zn vacancy. The g-values are found to be in the range of 2.08797–2.09218, where the maximum g-value is 2.09218 for 5% Co concentration. From these observed signals, it can be credited to the Zn vacancy in the structure, which may have a crucial effect on the mag-
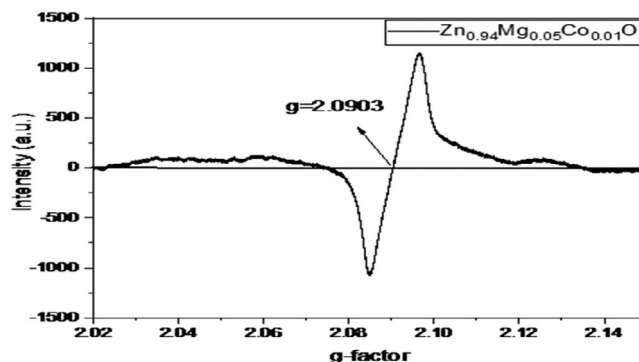
FIGURE 19 Calculated g-factor by using ESR spectra of $Zn_{0.94}Mg_{0.05}Co_{0.01}O$ nanoparticles. ESR, electron spin resonance.

netic behavior of ZnMgCoO NPs. Therefore, ZnMgCoO NPs can exhibit FM properties at RT. FM is investigated by the development of defects such as Zn interstitial (Zn_i) and Zn vacancy V_{Zn} which are observed from the PL measurement. Moreover, we also calculated the g-values corresponding to the tail of the ESR spectra and found that $g < 2$ which is due to the oxygen vacancy in the structure. Table 4 shows that the critical concentration of cobalt is 0.02 for maximum line-width and minimum g-factor.
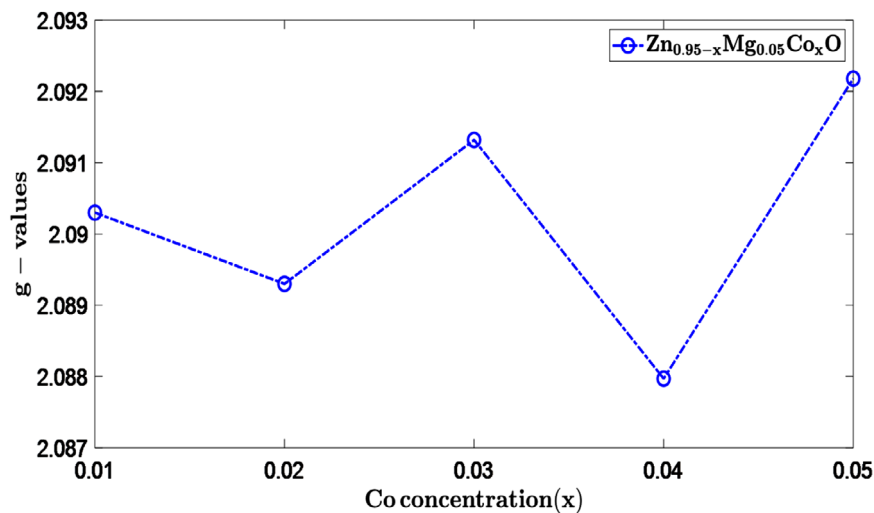
FIGURE 20 The g-values of ESR spectra of $Zn_{0.95-x}Mg_{0.05}Co_xO$ ($x = 0.01-0.05$) nanoparticles vs. Co concentrations.

4 | CONCLUSION

$Zn_{0.95-x}Mg_{0.05}Co_xO$ ($x = 0.01-0.05$ with an increment of 0.01) NPs were synthesized by the sol–gel technique. From PL measurements, Zn_i, V_{Zn}, and V_o defects were observed in Mg/Co co-doped NPs depending on the Co concentration in the visible region. These defects (zinc vacancies (V_{Zn}) and interstitial Zn (Zn_i) may have a crucial effect on the FM behavior of ZnMgCoO NPs at room temperature. By looking at the ESR spectra, the significant concentration of cobalt is 0.02 for minimum ΔH_{pp} and maximum g-factor. Notice that the ESR spectra for $x = 0.01-0.03$ were led by a robust and widest signal at nearby 324 mT except for $x = 0.04$ and 0.05. It was also found that the g-factor is between 2.08797 and 2.09218 which may be attributed to the zinc vacancy in the structure. However, in the ESR spectra, very small intensities were also observed and the g-values corresponding to those small intensities were less than 2 which may be attributed to the oxygen vacancy in the structure. The maximum and minimum g-factor values were 2.09218 and 2.08797 at $x = 0.05$ and $x = 0.42$, respectively.

As a result, the role of Mg dopants in improving the optical performance of ZnO and the role of the transition metal (Co) in enhancing the magnetic properties in addition to the intrinsic defects were observed.

ACKNOWLEDGMENTS

ORCID
Lutfi Arda https://orcid.org/0000-0003-0722-3891

REFERENCES
1. Yurish SY. Advances in microelectronics: reviews. Vol. 1. Barcelona: IFSA Publishing; 2018.

2. Noh MFM, Arzaee NA, Safaei J, Mohamed NA, Kim HP, Yusoff ARM, et al. Eliminating oxygen vacancies in SnO2 films via aerosol-assisted chemical vapor deposition for perovskite solar cells and photoelectrochemical cells. J Alloys Compd. 2019;773:997–1008.

3. Ra Y-W, Choi K-S, Kim J-H, Hahn Y-B, Im Y-H. Fabrication of ZnO nanowires using nanoscale spacer lithography for gas sensors. Small. 2008;4:1105–9.

4. Webb JB, Williams DF, Buchanan M. Transparent and highly conductive films of ZnO prepared by refractive magnetron sputtering. Appl Phys Lett. 1981;39:640.

5. Ronning C, Gao PX, Ding Y, Wang ZL, Schwen D. Manganese-doped ZnO nanobelts for spintronics. Appl Phys Lett. 2004;84:783–85.

6. Wolf SA, Awschalom D, Buhrman RA, Daughton JM, Molnar SV, Roukes ML, et al. Spintronics: a spin-based electronics vision for the future. Science. 2001;294:1488.

7. Choi Y, Kang J, Hwang D, Park S. Electron devices, recent advances in ZnO-based light-emitting diodes. IEEE Trans Electron Devices. 2010;57:26.

8. Clarke DR, Ceramics V. Varistor ceramics. J Am Ceram Soc. 1999;82(3):485–502.

9. Brayner R, Ferrari-Iliou R, Brivois N, Djediat S, Benedetti MF, Fiévet F. et al. Toxicological impact studies based on Escherichia coli bacteria in ultrafine ZnO nanoparticles colloidal medium. Nano Lett. 2006;6:866–70.

10. Boyraz C, Dogan N, Arda L. Microstructure and magnetic behavior of (Mg/Ni) co-doped ZnO nanoparticles. Ceram Int. 2017;43(17):15986–91.

11. Tosun M, Arda L. Effect of temperature and film thickness on structural and mechanical properties of c-axis oriented $Zn_{0.95}Mg_{0.05}O$ thin films. Ceram Int. 2019;45(13):16234–43.

12. Duru IP, Ozugurlu E, Arda L. Size effect on magnetic properties of $Zn_{0.95-x}Mg_xNi_{0.05}O$ nanoparticles by Monte Carlo simulation. Ceram Int. 2019;45:5259–65.

13. Senol SD, Boyraz C, Ozugurlu E, Gungor A, Arda L. Band gap engineering of Mg doped ZnO nanorods prepared by a hydrothermal method. Cryst Res Technol. 2019;54(3):1800233.

14. Akcan D, Ozharar S, Ozugurlu E, Arda L. The effects of Co/Cu Co-doped ZnO thin films: an optical study. J Alloys Compd. 2019;797:253–61.

15. Doğan N, Bingölbali A, Arda L. Preparation, structure and magnetic characterization of Ni-doped ZnO nanoparticles. J Magn Magn Mater 2015;373:226–30.

16. Asikuzun E, Ozturk O, Arda L, Terzioglu C. Preparation, growth and characterization of nonvacuum Cu-doped ZnO thin films. J Mol Struct. 2018;1165:1–7.

17. Guler A, Arda L, Dogan N, Boyraz C, Ozugurlu E. The annealing effect on microstructure and ESR properties of (Cu/Ni) co-doped ZnO nanoparticles. Ceram Int. 2019;45(2):1737–45.

18. Arda L. The effects of Tb doped ZnO nanorod: an EPR study. J Magn Magn Mater. 2019;475:493–501.

19. Asikuzun E, Ozturk O, Arda L, Terzioglu C. Microstructural and electrical characterizations of transparent Er-doped ZnO nano-thin films prepared by sol–gel process. J Mater Sci: Mater Electron. 2017;28:14314–22.

20. Üzar N, Algün G, Akçay N, Akcan D, Arda L. Structural, optical, electrical and humidity sensing properties of (Y/Al) co-doped ZnO thin films. J Mater Sci: Mater Electron. 2017;28 11861–70.

21. Ahmad I, Akhtar MS, Ahmed E, Ahmad M. Facile synthesis of Pr-doped ZnO photocatalyst using sol-gel method and its visible-light photocatalytic activity. J Mater Sci Mater Electron. 2020;31(2):1084–93.

22. Heiba ZK, Arda L, Mohamed MB, Mostafa NY, Al-Jalali MA, Dogan N. Effect of annealing temperature on structural and magnetic properties of Zn0.94Co0.05Cu0.01O. J Superconduct Novel Magn. 2013;26:3299–304.

23. Pandiyarajan T, Udayabhaskar R, Karthikeyan B. Role of Fe doping on structural and vibrational properties of ZnO nanostructures. Appl Phys A. 2012;107:411–19.

24. Boyraz C, Doğan N, Arda L. Microstructure and magnetic behavior of (Mg/Ni) co-doped ZnO nanoparticles. Ceram Int. 2017;43:15986–91.

25. Asikuzun E, Donmez A, Arda L, Cakiroglu O, Ozturk O, Akcan D, et al. Structural and mechanical properties of (Co/Mg) co-doped nano ZnO. Ceram Int. 2015;41:6326–34.

26. Ohno H. Making nonmagnetic semiconductors ferromagnetic. Science. 1998;281:951–56.

27. Imam NG, Harfouche M, Azab AA, Solyman S. Coupling between γ-irradiation and synchrotron-radiation-based XAFS techniques for studying Mn-doped ZnO nanoparticles. J Synchrotron Radiat. 2022;29(5):1187–97.

28. Senol SD, Ozugurlu E, Arda L. The effect of cobalt and boron on the structural, microstructural, and optoelectronic properties of ZnO nanoparticles. Ceram Int. 2020;46:7033–44.

29. Dietl T. Ferromagnetic semiconductors. Semicond Sci Technol. 2002;17:377.

30. Chithira PR, John TT. Correlation among oxygen vacancy and doping concentration in controlling the properties of cobalt doped ZnO nanoparticles. J Magn Magn Mater. 2020;496:165928.

31. Zong Y, Sun Y, Meng S, Wang Y, Xing H, Li X, et al. Doping effect and oxygen defects boost room temperature ferromagnetism of Co-doped ZnO nanoparticles: experimental and theoretical studies. RSC Adv. 2019;9:23012–20.

32. Heiba ZK, Mohamed MB, and Imam NG. Defect based violet–blue emission of Mg doped ZnO annealed at different temperatures. J Mater Sci: Mater Electron. 2015;26:6344–51.

33. Azab AA, Esmail SA, Abdelamksoud MK. Studying the effect of cobalt doping on optical and magnetic properties of zinc oxide nanoparticles. Silicon. 2019;11(1):165–74.

34. Singh NK, Koutu V, Malik MM. Enhancement of room temperature ferromagnetic behavior of Co-doped ZnO nanoparticles synthesized via sol–gel technique. J Sol–Gel Sci Technol. 2019;91:324–34.

35. Pan H, Zhang Y, Hu Y, Xie H. Effect of cobalt doping on optical, magnetic and photocatalytic properties of ZnO nanoparticles. Optik. 2020;208:164560.

36. Siddheswaran R, Mangalaraja RV, Avila RE, Manikandan D, Jeyanthi CE, Ananthakumar S. Evaluation of mechanical hardness and fracture toughness of Co and Al co-doped ZnO. Mater Sci Eng A. 2012;558:456–61.

37. Vijayakumar S, Lee SH, Ryu KS. Hierarchical CuCo2O4 nanobelts as a supercapacitor electrode with high areal and specific capacitance. Electrochim Acta. 2015;182:979–86.

38. Amri A, Jiang ZT, Pryor T, Yin CY, Xie Z, Mondinos N. Optical and mechanical characterization of novel cobalt-based metal oxide thin films synthesized using sol–gel dip-coating method. Surf Coating Technol. 2012;207:367–74.

39. Amri A, Duan X, Yin CY, Jiang ZT, Rahman MM, Pryor T. Solar absorptance of copper–cobalt oxide thin film coatings with nano-size, grain-like morphology: optimization and synchrotron radiation XPS studies. Appl Surf Sci. 2013;275:127–35.

40. Heiba Z K, Arda L. XRD, XPS, optical, and Raman investigations of structural changes of nano Co-doped ZnO. J Mol Struct. 2012;1022:167–71.

41. Tamura T, Ozaki H. The relationship of the magnetic properties of M (M = Mn, Fe, Co)-doped ZnO single crystals and their electronic structures. J Condens Matter Phys. 2009;21(2):026009.

42. Ohtomo A, Kawasaki M, Koida T, Masubuchi K, Koinuma H. MgxZn1−xO as a II–VI widegap semiconductor alloy. Appl Phys Lett. 1998;72:2466.

43. Heiba ZK, Arda L. Structural properties of Zn1−xMgxO nano-materials prepared by sol–gel method. Cryst Res Technol. 2009;44:845–50.

44. Arda L, Acikgoz M, Dogan N, Akcan D, Cakiroglu O. Synthesis, characterization and ESR studies of Zn1−xCoxO nanoparticles. J Supercond Nov Magn. 2013;27:799–804.

45. Arda L, Acikgoz M, Heiba ZK, Dogan N, Akcan D, Cakiroglu O. Synthesis, characterization and ESR studies of powder Zn0.95−xMg0.05AlxO (x = 0.0, 0.01, 0.02, 0.05, and 0.1) nanocrystals. Solid State Commun. 2013;170:14–18.

46. Singh SC, Gopal R. Drop shaped zinc oxide quantum dots and their self-assembly into dendritic nanostructures: liquid assisted pulsed laser ablation and characterizations. Appl Surf Sci. 2012;258:2211–18.

47. Korkmaz M, Aktaş B. A fast computational method to obtain spin Hamiltonian parameters of S = 1/2 and I = 5/2 ions. Phys Stat Sol B. 1985;132:573.